

OPAL: Visibility-aware LiDAR-to-OpenStreetMap Place Recognition via Adaptive Radial Fusion

Shuhao Kang^{1*}, Martin Y. Liao^{2*}, Yan Xia^{1†}, Olaf Wysocki¹, Boris Jutzi¹, Daniel Cremers¹

¹ Technical University of Munich

² Wuhan University

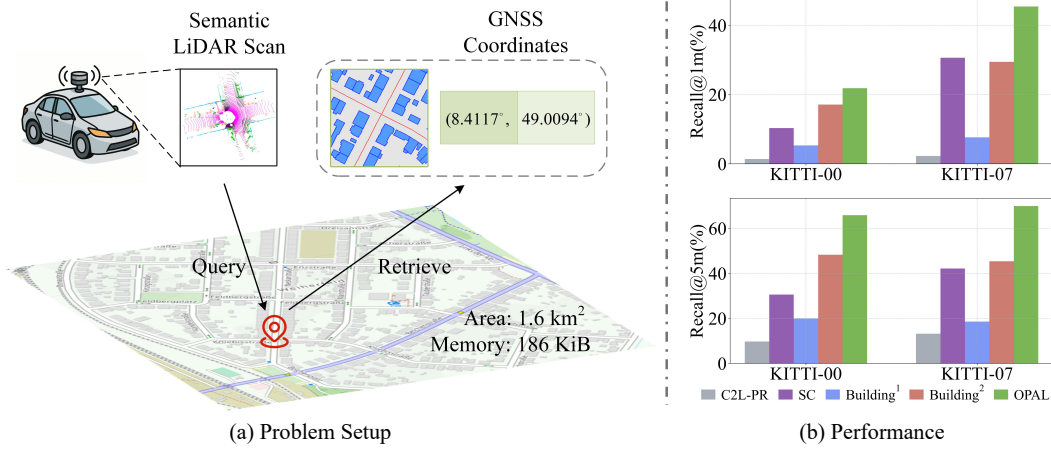


Figure 1: (a) Point cloud-to-OpenStreetMap (P2O) place recognition estimates the geographic location of a LiDAR scan by matching semantic point clouds to geo-referenced OpenStreetMap (OSM) tiles. (b) shows the evaluation results on the KITTI dataset.

Abstract: LiDAR place recognition is a critical capability for autonomous navigation and cross-modal localization in large-scale outdoor environments. Existing approaches predominantly depend on pre-built 3D dense maps or aerial imagery, which impose significant storage overhead and lack real-time adaptability. In this paper, we propose OPAL, a novel network for LiDAR place recognition that leverages OpenStreetMap as a lightweight and up-to-date prior. Our key innovation lies in bridging the domain disparity between sparse LiDAR scans and structured OSM data through two carefully designed components: a cross-modal visibility mask that identifies maximal observable regions from both modalities to guide feature learning, and an adaptive radial fusion module that dynamically consolidates multiscale radial features into discriminative global descriptors. Extensive experiments on the augmented KITTI and KITTI-360 datasets demonstrate OPAL’s superiority, achieving 15.98% higher recall at @1m threshold for top-1 retrieved matches while operating at 12× faster inference speeds compared to state-of-the-art approaches. Code and datasets are publicly available at: <https://github.com/WHU-USI3DV/OPAL>.

Keywords: Place Recognition, Multi-modality, OpenStreetMap, Point Cloud

1 Introduction

Accurate and reliable localization is crucial for autonomous vehicles and robots operating in large-scale urban environments, where GNSS signals are often degraded or blocked due to structural

*Equal contribution.

obstructions. Place recognition addresses this need by retrieving the most likely location from a reference database, based on a query that reflects the robot’s current perception. Compared with image-based place recognition methods [1, 2, 3], which suffer from photometric variations caused by changing weather and seasons [4], LiDAR point clouds maintain robustness under varying illumination and meteorological conditions. Moreover, point cloud offers precise depth measurements and rich geometric detail, making them effective for accurate localization in outdoor environments [5, 6].

Most existing point cloud-based place recognition methods rely on pre-built 3D maps [7, 8, 9, 10] or satellite images [11] as reference databases. However, constructing a city-scale point cloud map is both time-consuming and costly to maintain, while storage demands remain prohibitively high for large-scale deployments. Although aerial images are more compact than 3D point cloud maps, they are still expensive to capture, generally not free, and still heavy to store at high resolution. Moreover, they are highly sensitive to weather, seasonal changes, and lighting conditions. In contrast, OpenStreetMap (OSM) provides a globally accessible, compact geospatial database comprising infrastructure, architectural elements, points of interest, land-use classifications and other stationary urban features [12]. Its rich geometric primitives and semantic elements enable robust place recognition, mirroring human navigation’s use of spatial and semantic cues [13, 14]. Cho et al. [15] developed a place recognition descriptor by calculating the shortest distances to building structures at fixed angular intervals around the sensor. While Lee and Ryu [16] later extended this method for sequential point cloud place recognition, their method requires an accurate orientation prior for initialization. Overall, current single-frame P2O place recognition research remains limited in accuracy, robustness and efficiency.

In this paper, we present OPAL, a novel P2O place recognition framework that achieves meter-level localization accuracy using single LiDAR scans while maintaining real-time computational performance. The OPAL pipeline begins by projecting the query point cloud and OSM data into a polar bird’s-eye view (BEV) representation and generating a visibility mask as an additional input to alleviate viewpoint disparity. A Siamese convolutional neural network (CNN) then processes these polar representations to extract local feature maps. Then, the adaptive radial fusion (ARF) module is introduced to dynamically weight radial-wise features based on their contextual importance, enabling optimized feature aggregation across varying distances and robustness to view change. Experiments on the KITTI and KITTI-360 datasets demonstrate that our method significantly outperforms both hand-crafted and learning-based baselines across various environments. The main contributions include:

1. We propose a novel learning-based pipeline for P2O place recognition. Compared to existing methods, our approach substantially improves accuracy, robustness, and computational efficiency.
2. We introduce the visibility mask to resolve the viewpoint disparity between cross-modal inputs. The visibility mask significantly improves cross-modality feature alignment by focusing on mutually visible regions and ignoring modality-specific occlusions.
3. We propose the ARF module to dynamically fuse radial features into the global descriptor. This adaptive strategy preserves geometric structure while maintaining real-time efficiency.

2 Related Work

We review point cloud place recognition research through two perspectives: unimodal point cloud place recognition approaches and cross-modality approaches that bridge different sensor domains.

Unimodal Point cloud place recognition. Early breakthroughs in point cloud-to-point cloud place recognition were led by PointNetVLAD [7], which combined PointNet [17] with the NetVLAD [7] aggregation layer to produce global descriptors from raw point clouds. Transformer-based architectures have also been explored for capturing long-range dependencies and contextual semantics [18, 19, 20], leveraging attention mechanisms to improve feature expressiveness. MinLoc3D [21] employed a voxel-FPN architecture with generalized mean pooling (GeM) for com-

pact global descriptors. More recently, CASSPR [22] proposed a hybrid voxel-point dual-branch framework using hierarchical cross-attention to effectively fuse multi-level features, significantly boosting performance on sparse single-frame scans. Although these methods leverage the rich spatial information from LiDAR data to achieve strong performance, their scalability is restricted by the high cost and maintenance overhead associated with constructing and updating dense, city-scale point cloud maps. These practical limitations pose a major obstacle to large-scale deployment in consumer-grade applications.

Cross-Modality Point Cloud Place Recognition. For image-to-point cloud place recognition, Cataneo et al. [23] and Li et al. [24] established a shared global feature space for feature matching and retrieval. C2L-PR [25] improved cross-modality matching via modality alignment and orientation voting. For LiDAR-to-aerial image place recognition, Tang et al. [11] proposed a self-supervised localization approach based on 2D occupancy map matching. Beyond image-LiDAR matching, recent efforts have extended cross-modal localization to natural language queries [26, 27, 28].

OpenStreetMap-based approaches are most related to our method. OpenStreetSLAM [29] integrated visual odometry with map priors to improve trajectory accuracy, while subsequent methods [30, 31] focused on aligning the road or building geometries with OSM layouts. Suger and Burgard [32] introduced a Monte Carlo localization framework that aligns semantic features from LiDAR with the OSM data for outer-urban navigation. Building on semantic cues, Yan et al. [33] proposed a compact 4-bit descriptor that encodes building topology patterns for efficient global localization. Similarly, Bieringer et al. [34] utilized facade-rich level of detail 3 (LOD-3) models for outdoor map-based positioning. Above methods are fundamentally tailored for sequential point cloud localization and struggle with single-frame place recognition with limited information. For the single-frame point cloud-to-OpenStreetMap place recognition, Cho et al. [15] pioneered a hand-crafted descriptor by extracting the shortest distance to buildings at fixed angular intervals for cross-modality feature matching, later improved by Li et al. [35] with directional boundary features. However, these methods remain fundamentally limited by their heavy reliance on building structures, resulting in compromised accuracy and robustness and efficiency. Though Lee and Ryu [16] explored learning-based descriptors, their reliance on prebuilt submaps and IMU-based orientation priors limits scalability. To summarize, existing solutions suffer from three key limitations: reliance on sequential inputs, limited accuracy and robustness, and inefficient descriptor generation. To address these challenges, we propose OPAL, a learning-based P2O place recognition framework that captures a unified representation of geometry and topology, enabling accurate, robust, and generalizable localization across diverse environments.

3 Methodology

The point cloud-to-OpenStreetMap (P2O) place recognition aims to localize a query LiDAR point cloud $\mathcal{P} \in \mathbb{R}^{N \times 3}$ by matching it against a geo-referenced OSM database \mathbb{O} , where each of the N points in \mathcal{P} is represented by a 3D Cartesian coordinate (x, y, z) . Since our approach incorporates cross-modality data, \mathcal{P} and \mathbb{O} require pre-processing before being fed into the framework. \mathcal{P} is first enhanced by concatenating per-point semantic labels as $\mathcal{P}' \in \mathbb{R}^{N \times 4}$. The original OSM data \mathbb{O} is stored in structured metadata and represents the areas, ways and nodes with the region of interest (ROI), as well as polylines and point of interest (POI) in the geographic coordinate system. Following the OrienterNet [13], we rasterize the areas, ways, and nodes into a 3-channel grid map with a fixed sampling distance Δ in the local 2D East-North coordinate system. From this projected map, we densely sample m OSM reference tiles $\mathbb{O} = \{\mathcal{O}_i\}_{i=1}^m$ along the ego-vehicle trajectory, where each tile \mathcal{O}_i corresponds to an $H \times W$ meters region centered at geographic coordinates $(lat, lon)_i$.

Fig. 2 illustrates the OPAL framework’s processing pipeline. The pipeline begins by computing visibility masks to resolve occlusion patterns caused by viewpoint disparities (Sec. 3.1). Next, we employ a Siamese polar CNN architecture to extract deep feature maps from both modalities (Sec. 3.2), which are subsequently aggregated into compact global descriptors through the proposed adaptive radial fusion module (Sec. 3.3).

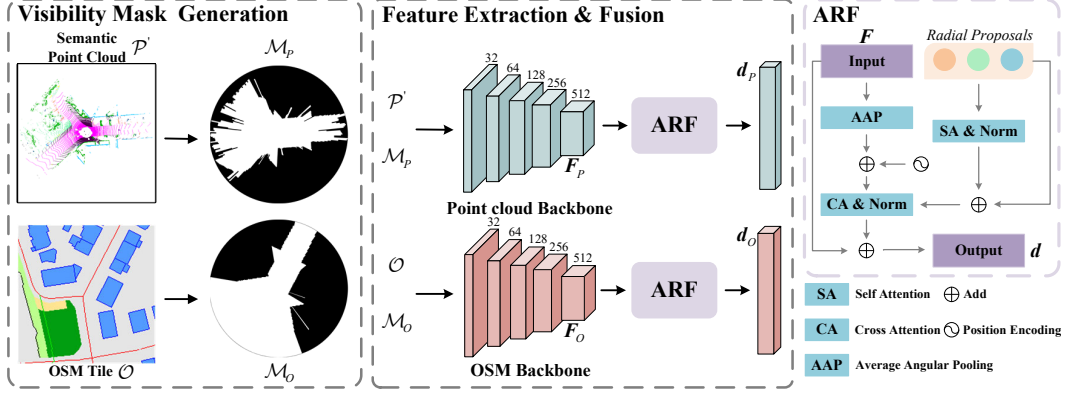


Figure 2: Overview of our proposed OPAL. Given a semantic point cloud frame \mathcal{P}' and OSM tile \mathcal{O} , OPAL computes visibility masks to bridge the occlusion bias, then extracts polar BEV features via a Siamese encoder, and lastly generates discriminative descriptors using adaptive radial fusion (ARF) for efficient place retrieval.

3.1 Visibility Mask Generation

The concept of visibility alignment originates from prior work in occlusion handling for image matching [36], visual localization [11, 13], and 3D building reconstruction [37]. In the P2O place recognition, this challenge is particularly pronounced due to the modality gap between LiDAR scans and OSM data, as well as potential temporal discrepancies in data collection. Effective visibility handling becomes crucial for robust cross-modal matching.

To address this challenge, we compute separate visibility masks \mathcal{M} for both point cloud and OSM data to resolve occlusion discrepancies. Given a point cloud frame $\mathcal{P}' \in \mathbb{R}^{N \times 4}$, we first project it onto a polar BEV grid with U radial rings and V angular sectors, aggregating points within each cell (u, v) . The radial and angular resolutions are given by $\Delta_r = \frac{L}{U}$ and $\Delta_s = \frac{2\pi}{V}$, where L is defined as the maximum valid range of LiDAR. For each polar cell (u, v) , the corresponding radial distance r_u and azimuth angle ϕ_v are defined as:

$$\begin{aligned} r_u &= (u + 0.5)\Delta_r, \quad u \in \{0, \dots, U - 1\}, \\ \phi_v &= (v + 0.5)\Delta_s, \quad v \in \{0, \dots, V - 1\}. \end{aligned} \quad (1)$$

Through ray casting, cells are classified as visible $\mathcal{M}_P(u, v) = 1$ if they lie within the line-of-sight before the last measured return in a sector. Conversely, cells are marked as occluded $\mathcal{M}_P(u, v) = 0$ if they are behind the last valid range return or beyond the sensor range L :

$$\mathcal{M}_P(u, v) = \begin{cases} 1, & \rho(u, v) \leq \rho_{\max}(v) \\ 0, & \text{otherwise} \end{cases} \quad (2)$$

where $\rho(u, v) = (u + 0.5)\Delta_r$ denotes the radial distance, and $\rho_{\max}(v)$ is range of last valid return in v -th sector.

For the OSM tile $\mathcal{O} \in \mathbb{R}^{H \times W \times 3}$ defined in the 2D Cartesian coordinate system, we convert it into a polar BEV grid with U rings and V sectors, as in the point cloud branch. For each polar cell (u, v) , the corresponding Cartesian coordinates (x_{uv}, y_{uv}) are computed via:

$$x_{uv} = r_u \cos \phi_v, \quad y_{uv} = r_u \sin \phi_v, \quad (3)$$

and the polar representation is obtained through bilinearly interpolation of \mathcal{O} at the computed (x_{uv}, y_{uv}) coordinates.

As OSM data lacks explicit range measurements, visibility estimation relies on semantic cues. Here, we select the building elements in the area channel as primary occluders due to their vertical extent and structural continuity, which consistently obstruct sensor visibility in urban and suburban environments. The visibility mask \mathcal{M}_O is computed by checking for occlusion along each radial

direction:

$$\mathcal{M}_O(u, v) = \begin{cases} 1, & \rho(u, v) \leq \rho(u', v) \text{ where } \mathcal{O}[u', v] = \text{“building”} \\ 0, & \text{otherwise} \end{cases} \quad (4)$$

where $\mathcal{O}(u', v)$ is the nearest building element in the v -th sector.

Remark: Unlike prior approaches [11, 13] that estimated the visible or confidential mask with a neural network, our visibility mask generation is fully deterministic and leverages the complementary strengths of both modalities. LiDAR offers accurate occlusion cues through precise depth and sensor geometry, while OSM provides structured semantic annotations that support topological reasoning. By avoiding the approximation errors and training overhead associated with learned visibility estimation, our approach preserves geometric consistency across modalities and ensures computational efficiency.

3.2 Feature Extraction

As shown in Fig. 2, our feature extraction pipeline processes both modalities through parallel yet symmetric branches. The augmented point cloud $P' \in \mathbb{R}^{N \times 4}$ first passes through a lightweight MLP to generate C_{pem} -dimensional per-point features. These features are then splatted onto the polar BEV grid and generate the grid-wise feature by max response (with `torch.scatter_max()` function in PyTorch implementation), yielding a dense feature map $F_P \in \mathbb{R}^{U \times V \times C_{pem}}$. This representation is concatenated with the visibility mask $\mathcal{M}_P \in \mathbb{R}^{U \times V \times 1}$, and processed by the encoder of PolarNet [38] to produce the final local feature map $F'_P \in \mathbb{R}^{Z \times T \times C}$.

The OSM branch processes the rasterized map tile $\mathcal{O} \in \mathbb{R}^{H \times W \times 3}$ through a symmetric pipeline. A MLP first embeds each semantic class of \mathcal{O} into a C_{oem} -channel vector, generating a dense semantic feature map $F_O \in \mathbb{R}^{H \times W \times (3 \times C_{oem})}$ in the Cartesian coordinate system, where each channel corresponds to distinct geographic elements. This embedded representation is transformed to a polar BEV feature map by bilinear sampling with Eq. (3) and concatenated with the visibility mask $\mathcal{M}_O \in \mathbb{R}^{U \times V \times 1}$ to form a visibility-aware input. The OSM features are processed through a separate PolarNet encoder (with weights independent of the point cloud branch) to produce the final feature map $F'_O \in \mathbb{R}^{Z \times T \times C}$.

3.3 Adaptive Radial Fusion

The local features $F \in \mathbb{R}^{Z \times T \times C}$ from the point cloud or OSM tiles require representative and rotation-robust aggregation into global descriptors. Existing solutions face critical trade-offs: frequency-domain methods [39, 40] and range projections [20] sacrifice spatial relationships for rotation invariance, while sampling-based approaches like BEVPlace++ [10] incur excessive computational costs. These limitations prove prohibitive for cross-modality place recognition, compromising geometric fidelity or system efficiency.

To achieve both geometric completeness and rotation robustness, we introduce the adaptive radial fusion (ARF) module (shown in the last column of Fig. 2). The module first extracts radial features through angular average pooling (AAP):

$$F_r = \frac{1}{T} \sum_{t=1}^T F[:, t, :] + E_{re}, \quad (5)$$

where F_r represents the radially compressed features, and $E_{re} \in \mathbb{R}^{Z \times C}$ encodes the ring-order information using cosine position encoding [41]. Building upon the radial-wise features, we introduce trainable *radial proposals* $Q \in \mathbb{R}^{Z \times C}$ as in [42, 43] to track and fuse the radial-wise features based on significance adaptively. The *radial proposals* are implemented as trainable model parameters (via `nn.Parameters()` in PyTorch implementation) that undergo a two-stage attention refinement process. First, inter-proposal communication is enhanced with a self-attention module:

$$Q' = \text{softmax}\left(\frac{QQ^\top}{\sqrt{C}}\right)Q. \quad (6)$$

This allows the proposals to develop global contextual awareness while suppressing redundant correlations. The refined proposals then perform selective feature aggregation through cross-attention with the radial features:

$$\mathbf{F}'_r = \text{softmax}\left(\frac{\mathbf{Q}'\mathbf{F}_r^\top}{\sqrt{C}}\right)\mathbf{F}_r. \quad (7)$$

This attention mechanism dynamically weights the contribution of each radial feature based on its geometric salience for place recognition, effectively focusing on discriminative spatial patterns while maintaining robustness to viewpoint variations. The refined radial features \mathbf{F}'_r are combined with the original \mathbf{F}_r via residual connection and transformed into the global descriptor \mathbf{d} :

$$\mathbf{d} = \mathbf{W}(\text{Flatten}(\mathbf{F}_r + \mathbf{F}'_r)), \quad (8)$$

where $\text{Flatten}(\cdot)$ denotes the flattening operation that converts the radial-wise features into a 1D vector, and \mathbf{W} is a fully connected layer that maps this vector to the global descriptor \mathbf{d} .

Remark: The ARF module’s key innovation lies in combining LiDAR’s native radial geometry with learned attention. Angular average pooling preserves the sensor’s scanning pattern while ensuring rotation robustness, and the trainable radial proposals adaptively weight features by both geometric and semantic importance. This dual approach surpasses fixed aggregation methods without compromising computational efficiency.

4 Experiments

4.1 Experimental setup

We validate the proposed method on two public datasets: KITTI [44] and KITTI-360 [45] datasets. The corresponding OSM data is collected from the OpenStreetMap official website*. Our model is trained exclusively on the KITTI dataset and evaluated in a zero-shot setting on KITTI-360 to assess its generalization capability. For evaluation, we adopt the standard Recall@ K m metric, which measures the proportion of queries whose top-1 retrieved match falls within K -meters of the ground-truth (GT) location. More details about the complementary datasets are provided in Appendix A.

Baseline methods: Due to the limited attention of P2O place recognition research, we adapt three representative baselines for fair comparison: a) Building [15]: the pioneering P2O place recognition method that first utilizes a global key for fast matching, followed by a fine-grained descriptor for precise localization. We re-implement both the original two-stage version (Building²) and a simplified one-stage variant (Building¹) for comparison. b) SC [46]: a widely-used point cloud-to-point cloud place recognition method based on hand-crafted descriptors. Following Li et al. [35], we generate virtual building points from both LiDAR scans and OSM data to facilitate descriptor extraction and matching. c) C2L-PR [25]: A hybrid framework for image-to-point cloud place recognition. C2L-PR first extracts hand-crafted features from point cloud semantics (road, parking, sidewalk, other-ground, building, fence, other-structure, vegetation, terrain) and OSM data (building, parking, grass, forest, fence, wall, road), then learns the descriptors via an embedding network.

4.2 Place Recognition Results

KITTI. As shown in Tab. 1, OPAL demonstrates superior place recognition performance on KITTI sequences 00 and 07, outperforming all baseline methods by a large margin. Specifically, it achieves significant improvements of 4.73%, 17.55%, and 17.47% in R@1m/5m/10m metrics on sequence 00, and 15.98%, 24.53%, and 24.52% on sequence 07 compared to state-of-the-art method, Building² [15]. Fig. 3 illustrates OPAL’s accurate localization results along the trajectory across diverse environments, highlighting OPAL’s robust performance under different conditions. These results collectively validate OPAL’s effectiveness in enhancing both localization accuracy and robustness, as reflected by consistent improvements across all evaluation metrics.

*<https://www.openstreetmap.org/>

Table 1: Recall@ K m of top-1 retrieved results on the KITTI dataset.

OPAL-Rot: OPAL with randomly rotated queries.						
Method	Seq 00			Seq 07		
	R@1	R@5	R@10	R@1	R@5	R@10
SC [46]	10.31	30.54	31.16	30.61	42.42	43.42
Building ¹ [15]	5.31	19.89	20.52	7.63	18.53	19.35
Building ² [15]	17.09	48.23	48.93	29.43	45.32	45.78
C2L-PR [25]	1.39	9.69	12.20	2.27	13.17	17.26
OPAL	21.82	65.78	66.40	45.41	69.85	70.30
OPAL-Rot	21.49	66.46	67.14	46.14	70.12	70.30

Table 2: Ablation study on visibility mask and ARF module.

VM: visibility mask; FA: feature aggregation.

ID	VM	FA	R@1	R@5	R@10
[A]		GAP	3.79	22.46	24.82
[B]		ARF	21.03	62.21	63.27
[C]	✓	GAP	5.84	17.95	19.18
[D]	✓	GeM	1.56	9.36	10.52
[E]	✓	VLAD	6.39	30.70	32.26
[F]	✓	AAP	17.68	51.62	52.17
[G]	✓	ARF	21.82	65.78	66.40

Table 3: Recall@ K m of top-1 retrieved results on the KITTI-360 dataset.

Method	Seq 00			Seq 05			Seq 06			Seq 09		
	R@1	R@5	R@10	R@1	R@5	R@10	R@1	R@5	R@10	R@1	R@5	R@10
SC [46]	15.14	39.61	40.66	3.69	16.69	17.18	4.14	14.22	14.59	13.92	27.45	28.07
Building ¹ [15]	5.22	15.76	17.07	0.87	3.91	4.61	0.60	3.18	3.79	4.21	12.16	13.27
Building ² [15]	17.12	49.61	51.29	4.23	15.94	16.29	3.00	12.82	13.39	18.28	41.92	42.64
C2L-PR [25]	1.70	8.23	10.93	0.81	4.72	6.36	0.45	3.35	4.50	1.69	9.59	12.45
OPAL	14.92	42.82	44.18	7.74	30.49	31.55	7.71	36.38	37.54	27.89	60.96	61.92

Table 4: Descriptor generation runtime (ms).

Method	Point Cloud	OSM Tile	Total
SC [46]	37.58	17.09	54.67
Building [15]	29.86	54.87	84.73
C2L-PR [25]	219.08	316.71	535.79
OPAL	1.91	5.14	7.05

Table 5: Influence of Semantic label in point cloud.

Semantic Label	R@1	R@5	R@10
Rangenet++ [47]	18.92	59.08	60.30
Cylinder3D [48]	21.82	65.78	66.40
Ground Truth [49]	25.37	73.99	74.68

Robust to rotation. To assess rotational robustness, we apply random z-axis rotations ($0 \sim 2\pi$) to each query point cloud to simulate view change. As shown in the last row of Tab. 1, OPAL remains robust under these transformations, validating the robustness of our pipeline.

Zero-shot Generalization on KITTI-360. As shown in Tab. 3, while OPAL shows slightly reduced performance in building-dominated urban environments (sequence 00) compared to the Building² [15], it achieves significant improvements over baselines in other sequences (05, 06, 09), with performance gains of 14.55%, 23.56%, and 19.04% at R@5m, respectively. Fig. 4 presents the recall curves of top candidates within a 5-meter threshold on the KITTI and KITTI-360 datasets, where our OPAL consistently outperforms baseline methods across diverse scenes. These results highlight OPAL’s strong generalization capability across diverse environments.

Runtime Performance. We evaluated our method on a desktop with an Intel i9-13900K CPU and NVIDIA RTX 4090 GPU and reported the results in Tab. 4. Our OPAL achieves high efficiency, processing point clouds in 1.91ms and OSM tiles in 5.14ms, resulting in a total runtime of only 7.05ms. This corresponds to a throughput exceeding 140 FPS for descriptor generation, enabling deployment in time-sensitive applications.

4.3 Ablation Study

We conduct ablation studies on KITTI sequence 00 to evaluate the impact of three key components in OPAL: the visibility mask, ARF module, and semantic label of the point cloud.

Visibility mask and ARF. Tab. 2 presents a systematic comparison of seven architectural variants. Variant [A] removes the visibility mask and replaces ARF with global average pooling (GAP), while [B] introduces ARF alone, yielding notable performance gains. Variants [C], [D], and [E]



Figure 3: Top-1 retrieved results @5m threshold on the 00 sequence of the KITTI dataset. Red point ● notes the wrong retrieved result and green point ● notes the corrected retrieved result.

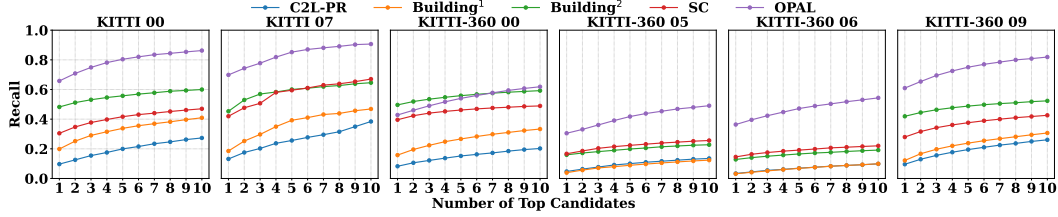


Figure 4: Recall curves @5m of top-10 candidates on the KITTI and KITTI-360 datasets.

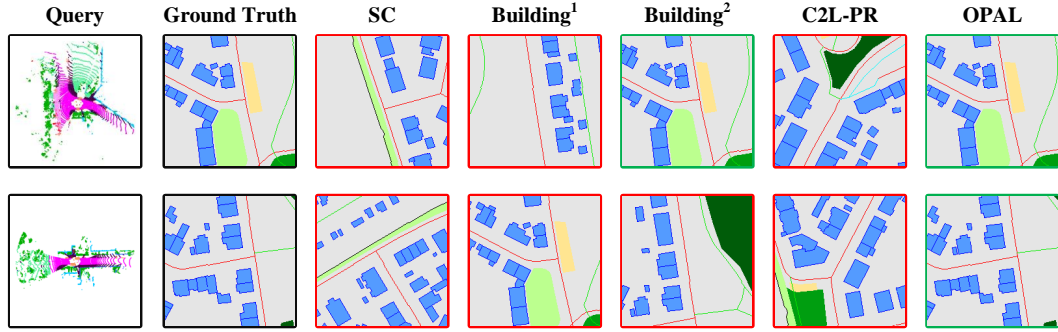


Figure 5: Examples of Lidar queries and their top-1 retrieved matches on KITTI. The red rectangle □ represents the wrong retrieved result and the green □ represents the correct retrieved result.

explore alternative aggregation strategies: GAP, GeM, and vector of locally aggregated descriptors (VLAD), respectively, while all of them perform poorly to match the corresponding OSM tile. $[F]$ employs the average angular pooling (AAP) for feature aggregation and achieves moderate performance. Finally, variant $[G]$ combines both the visibility mask and ARF module, achieving the best performance, confirming the effectiveness of their joint contribution.

Influence of semantic label in point cloud. Tab. 5 illustrates the impact of semantic labels on P2O place recognition performance. With the ground truth labels [49], our OPAL achieve the best results (74.68% R@10m), followed by predicted labels from Cylinder3D [48] (66.4%) and Rangenet++ [47] (60.30%). The 14.38% performance gap between RangeNet++ and GT annotations underscores the strong dependence of the framework’s accuracy on the precision of semantic labels within the point cloud.

5 Conclusion

In this work, we presented OPAL, a novel single-frame P2O place recognition framework. The proposed method introduces the visibility-aware mask to resolve the cross-modality occlusion, coupled with the adaptive radial fusion module for effectively and robustly global descriptor aggregation. Experiments on the KITTI and KITTI-360 datasets demonstrate that OPAL consistently outperforms state-of-the-art baseline methods across diverse challenging scenarios, achieving significant improvements in both accuracy and computational efficiency. We hope that our OPAL will benefit the relevant communities in the field.

6 Limitation

The localization accuracy of our OPAL heavily depends on the quality and distinctiveness of the surrounding objects in the point cloud. Fig. 6 shows some failure cases under different conditions. (a)-(b) demonstrate ambiguous scenarios at road crossings with limited distinctive features, resulting in top-1 retrieval errors due to the geometric similarity between the retrieved and ground-truth locations. As shown in (c)-(d), cross-modal discrepancies occur when roadside vegetation and buildings detected in LiDAR scans lacks equivalent features in OSM data. To address these limitations, we plan to extend OPAL to sequential point cloud-based place recognition, which could leverage temporal and geometric consistency to improve recognition reliability and accuracy.

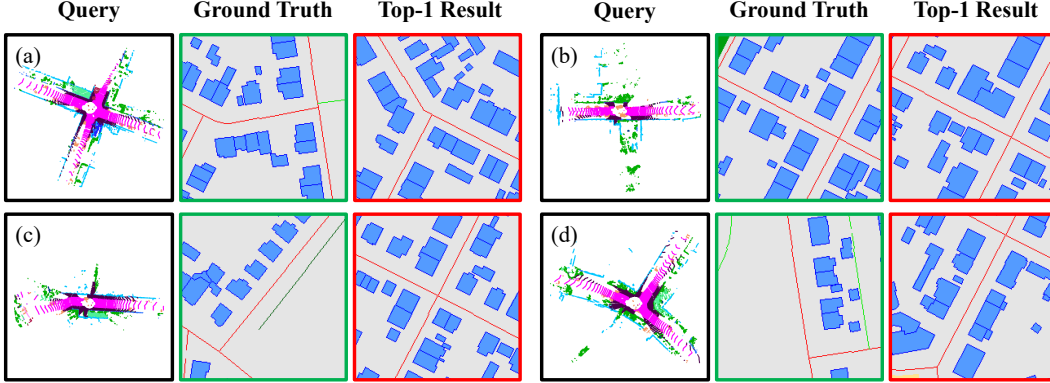


Figure 6: Failure cases. The red rectangle represents the wrong retrieved top-1 result and the green rectangle represents the GT OSM tile.

References

- [1] R. Arandjelovic, P. Gronat, A. Torii, T. Pajdla, and J. Sivic. Netvlad: Cnn architecture for weakly supervised place recognition. In *Proceedings of the IEEE conference on computer vision and pattern recognition*, pages 5297–5307, 2016.
- [2] S. Hausler, S. Garg, M. Xu, M. Milford, and T. Fischer. Patch-netvlad: Multi-scale fusion of locally-global descriptors for place recognition. In *Proceedings of the IEEE/CVF conference on computer vision and pattern recognition*, pages 14141–14152, 2021.
- [3] S. Zhu, L. Yang, C. Chen, M. Shah, X. Shen, and H. Wang. R2former: Unified retrieval and reranking transformer for place recognition. In *Proceedings of the IEEE/CVF Conference on Computer Vision and Pattern Recognition*, pages 19370–19380, 2023.
- [4] J. Yu, H. Ye, J. Jiao, P. Tan, and H. Zhang. Gv-bench: Benchmarking local feature matching for geometric verification of long-term loop closure detection. In *2024 IEEE/RSJ International Conference on Intelligent Robots and Systems (IROS)*, pages 7922–7928. IEEE, 2024.
- [5] Y. Xia, Y. Xu, C. Wang, and U. Stilla. Vpc-net: Completion of 3d vehicles from mls point clouds. *ISPRS Journal of Photogrammetry and Remote Sensing*, 174:166–181, 2021.
- [6] X. Chen, T. Labe, A. Milioto, T. Rohling, O. Vysotska, A. Haag, J. Behley, and C. Stachniss. Overlapnet: Loop closing for lidar-based slam. *Robotics: Science and Systems XVI*, 2020.
- [7] M. A. Uy and G. H. Lee. Pointnetvlad: Deep point cloud based retrieval for large-scale place recognition. In *Proceedings of the IEEE conference on computer vision and pattern recognition*, pages 4470–4479, 2018.

- [8] Z. Liu, S. Zhou, C. Suo, P. Yin, W. Chen, H. Wang, H. Li, and Y.-H. Liu. Lpd-net: 3d point cloud learning for large-scale place recognition and environment analysis. In *Proceedings of the IEEE/CVF international conference on computer vision*, pages 2831–2840, 2019.
- [9] Y. Xia, Y. Xu, S. Li, R. Wang, J. Du, D. Cremers, and U. Stilla. Soe-net: A self-attention and orientation encoding network for point cloud based place recognition. In *Proceedings of the IEEE/CVF Conference on computer vision and pattern recognition*, pages 11348–11357, 2021.
- [10] L. Luo, S.-Y. Cao, X. Li, J. Xu, R. Ai, Z. Yu, and X. Chen. Bevplace++: Fast, robust, and lightweight lidar global localization for unmanned ground vehicles. *arXiv preprint arXiv:2408.01841*, 2024.
- [11] T. Y. Tang, D. De Martini, and P. Newman. Get to the point: Learning lidar place recognition and metric localisation using overhead imagery. *Proceedings of Robotics: Science and Systems, 2021*, 2021.
- [12] H. Fan, A. Zipf, Q. Fu, and P. Neis. Quality assessment for building footprints data on open-streetmap. *International Journal of Geographical Information Science*, 28(4):700–719, 2014.
- [13] P.-E. Sarlin, D. DeTone, T.-Y. Yang, A. Avetisyan, J. Straub, T. Malisiewicz, S. R. Buló, R. Newcombe, P. Kotschieder, and V. Balntas. Orienternet: Visual localization in 2d public maps with neural matching. In *Proceedings of the IEEE/CVF Conference on Computer Vision and Pattern Recognition*, pages 21632–21642, 2023.
- [14] Y. Liao, X. Chen, S. Kang, J. Li, Z. Dong, H. Fan, and B. Yang. Osmloc: Single image-based visual localization in openstreetmap with geometric and semantic guidances. *arXiv preprint arXiv:2411.08665*, 2024.
- [15] Y. Cho, G. Kim, S. Lee, and J.-H. Ryu. Openstreetmap-based lidar global localization in urban environment without a prior lidar map. *IEEE Robotics and Automation Letters*, 7(2): 4999–5006, 2022.
- [16] S. Lee and J.-H. Ryu. Autonomous vehicle localization without prior high-definition map. *IEEE Transactions on Robotics*, 2024.
- [17] C. R. Qi, H. Su, K. Mo, and L. J. Guibas. Pointnet: Deep learning on point sets for 3d classification and segmentation. In *Proceedings of the IEEE conference on computer vision and pattern recognition*, pages 652–660, 2017.
- [18] Z. Fan, Z. Song, H. Liu, Z. Lu, J. He, and X. Du. Svt-net: Super light-weight sparse voxel transformer for large scale place recognition. In *Proceedings of the AAAI conference on artificial intelligence*, volume 36, pages 551–560, 2022.
- [19] W. Zhang, H. Zhou, Z. Dong, Q. Yan, and C. Xiao. Rank-pointretrieval: Reranking point cloud retrieval via a visually consistent registration evaluation. *IEEE Transactions on Visualization and Computer Graphics*, 2022.
- [20] J. Ma, J. Zhang, J. Xu, R. Ai, W. Gu, and X. Chen. Overlaptransformer: An efficient and yaw-angle-invariant transformer network for lidar-based place recognition. *IEEE Robotics and Automation Letters*, 7(3):6958–6965, 2022.
- [21] J. Komorowski. Minkloc3d: Point cloud based large-scale place recognition. In *Proceedings of the IEEE/CVF Winter Conference on Applications of Computer Vision*, pages 1790–1799, 2021.
- [22] Y. Xia, M. Gladkova, R. Wang, Q. Li, U. Stilla, J. F. Henriques, and D. Cremers. Casspr: Cross attention single scan place recognition. In *Proceedings of the IEEE/CVF international conference on computer vision*, pages 8461–8472, 2023.

- [23] D. Cattaneo, M. Vaghi, S. Fontana, A. L. Ballardini, and D. G. Sorrenti. Global visual localization in lidar-maps through shared 2d-3d embedding space. In *2020 IEEE International Conference on Robotics and Automation (ICRA)*, pages 4365–4371. IEEE, 2020.
- [24] Y.-J. Li, M. Gladkova, Y. Xia, R. Wang, and D. Cremers. Vxp: Voxel-cross-pixel large-scale image-lidar place recognition. In *2025 International Conference on 3D Vision (3DV)*, 2025.
- [25] H. Xu, H. Liu, S. Huang, and Y. Sun. C2l-pr: Cross-modal camera-to-lidar place recognition via modality alignment and orientation voting. *IEEE Transactions on Intelligent Vehicles*, 2024.
- [26] M. Kolmet, Q. Zhou, A. Ošep, and L. Leal-Taixé. Text2pos: Text-to-point-cloud cross-modal localization. In *Proceedings of the IEEE/CVF Conference on Computer Vision and Pattern Recognition*, pages 6687–6696, 2022.
- [27] Y. Xia, L. Shi, Z. Ding, J. F. Henriques, and D. Cremers. Text2loc: 3d point cloud localization from natural language. In *Proceedings of the IEEE/CVF Conference on Computer Vision and Pattern Recognition*, pages 14958–14967, 2024.
- [28] Y. Xia, Z. Li, Y.-J. Li, L. Shi, H. Cao, J. F. Henriques, and D. Cremers. Uniloc: Towards universal place recognition using any single modality. *arXiv preprint arXiv:2412.12079*, 2024.
- [29] G. Floros, B. Van Der Zander, and B. Leibe. Openstreetslam: Global vehicle localization using openstreetmaps. In *2013 IEEE international conference on robotics and automation*, pages 1054–1059. IEEE, 2013.
- [30] P. Ruchti, B. Steder, M. Ruhnke, and W. Burgard. Localization on openstreetmap data using a 3d laser scanner. In *2015 IEEE international conference on robotics and automation (ICRA)*, pages 5260–5265. IEEE, 2015.
- [31] O. Vysotska and C. Stachniss. Exploiting building information from publicly available maps in graph-based slam. In *2016 IEEE/RSJ International Conference on Intelligent Robots and Systems (IROS)*, pages 4511–4516. IEEE, 2016.
- [32] B. Suger and W. Burgard. Global outer-urban navigation with openstreetmap. In *2017 IEEE International Conference on Robotics and Automation (ICRA)*, pages 1417–1422. IEEE, 2017.
- [33] F. Yan, O. Vysotska, and C. Stachniss. Global localization on openstreetmap using 4-bit semantic descriptors. In *2019 European conference on mobile robots (ECMR)*, pages 1–7. IEEE, 2019.
- [34] A. Bieringer, O. Wysocki, S. Tuttas, L. Hoegner, and C. Holst. Analyzing the impact of semantic LoD3 building models on image-based vehicle localization. *ISPRS Annals of the Photogrammetry, Remote Sensing and Spatial Information Sciences*, 10:55–62, 2024.
- [35] Z. Li, Y. Wang, R. Zhang, F. Ding, C. Wei, and J.-G. Lu. A lidar-openstreetmap matching method for vehicle global position initialization based on boundary directional feature extraction. *IEEE Transactions on Intelligent Vehicles*, 2024.
- [36] M. Fan, M. Chen, C. Hu, and S. Zhou. Occ²net: Robust image matching based on 3d occupancy estimation for occluded regions. In *Proceedings of the IEEE/CVF International Conference on Computer Vision*, pages 9652–9662, 2023.
- [37] O. Wysocki, Y. Xia, M. Wysocki, E. Grilli, L. Hoegner, D. Cremers, and U. Stilla. Scan2LoD3: Reconstructing semantic 3D building models at LoD3 using ray casting and Bayesian networks. *IEEE/CVF Conference on Computer Vision and Pattern Recognition Workshops (CVPRW)*, pages 6547–6557, 2023.

- [38] Y. Zhang, Z. Zhou, P. David, X. Yue, Z. Xi, B. Gong, and H. Foroosh. Polarnet: An improved grid representation for online lidar point clouds semantic segmentation. In *Proceedings of the IEEE/CVF conference on computer vision and pattern recognition*, pages 9601–9610, 2020.
- [39] X. Xu, S. Lu, J. Wu, H. Lu, Q. Zhu, Y. Liao, R. Xiong, and Y. Wang. Ring++: Roto-translation invariant gram for global localization on a sparse scan map. *IEEE Transactions on Robotics*, 39(6):4616–4635, 2023.
- [40] S. Lu, X. Xu, L. Tang, R. Xiong, and Y. Wang. Deepring: Learning roto-translation invariant representation for lidar based place recognition. In *2023 IEEE International Conference on Robotics and Automation (ICRA)*, pages 1904–1911. IEEE, 2023.
- [41] A. Vaswani, N. Shazeer, N. Parmar, J. Uszkoreit, L. Jones, A. N. Gomez, Ł. Kaiser, and I. Polosukhin. Attention is all you need. *Advances in neural information processing systems*, 30, 2017.
- [42] N. Carion, F. Massa, G. Synnaeve, N. Usunier, A. Kirillov, and S. Zagoruyko. End-to-end object detection with transformers. In *European conference on computer vision*, pages 213–229. Springer, 2020.
- [43] A. Ali-Bey, B. Chaib-draa, and P. Giguère. Boq: A place is worth a bag of learnable queries. In *Proceedings of the IEEE/CVF Conference on Computer Vision and Pattern Recognition*, pages 17794–17803, 2024.
- [44] A. Geiger, P. Lenz, and R. Urtasun. Are we ready for autonomous driving? the kitti vision benchmark suite. In *2012 IEEE conference on computer vision and pattern recognition*, pages 3354–3361. IEEE, 2012.
- [45] Y. Liao, J. Xie, and A. Geiger. Kitti-360: A novel dataset and benchmarks for urban scene understanding in 2d and 3d. *IEEE Transactions on Pattern Analysis and Machine Intelligence*, 45(3):3292–3310, 2022.
- [46] G. Kim and A. Kim. Scan context: Egocentric spatial descriptor for place recognition within 3d point cloud map. In *2018 IEEE/RSJ International Conference on Intelligent Robots and Systems (IROS)*, pages 4802–4809. IEEE, 2018.
- [47] A. Milioto, I. Vizzo, J. Behley, and C. Stachniss. Rangenet++: Fast and accurate lidar semantic segmentation. In *2019 IEEE/RSJ international conference on intelligent robots and systems (IROS)*, pages 4213–4220. IEEE, 2019.
- [48] X. Zhu, H. Zhou, T. Wang, F. Hong, W. Li, Y. Ma, H. Li, R. Yang, and D. Lin. Cylindrical and asymmetrical 3d convolution networks for lidar-based perception. *IEEE Transactions on Pattern Analysis and Machine Intelligence*, 44(10):6807–6822, 2021.
- [49] J. Behley, M. Garbade, A. Milioto, J. Quenzel, S. Behnke, C. Stachniss, and J. Gall. Semantickitti: A dataset for semantic scene understanding of lidar sequences. In *Proceedings of the IEEE/CVF international conference on computer vision*, pages 9297–9307, 2019.
- [50] Y. Sun, C. Cheng, Y. Zhang, C. Zhang, L. Zheng, Z. Wang, and Y. Wei. Circle loss: A unified perspective of pair similarity optimization. In *Proceedings of the IEEE/CVF conference on computer vision and pattern recognition*, pages 6398–6407, 2020.

A Data pre-processing and details

A.1 Data pre-processing

We utilize Cylinder3D [48] to predict 19-class semantic labels (following SemanticKITTI [49]) for each query point cloud. For the KITTI-360 [45] dataset, we employ the KITTI-pretrained Cylinder3D model for semantic label prediction, enabling zero-shot place recognition evaluation.

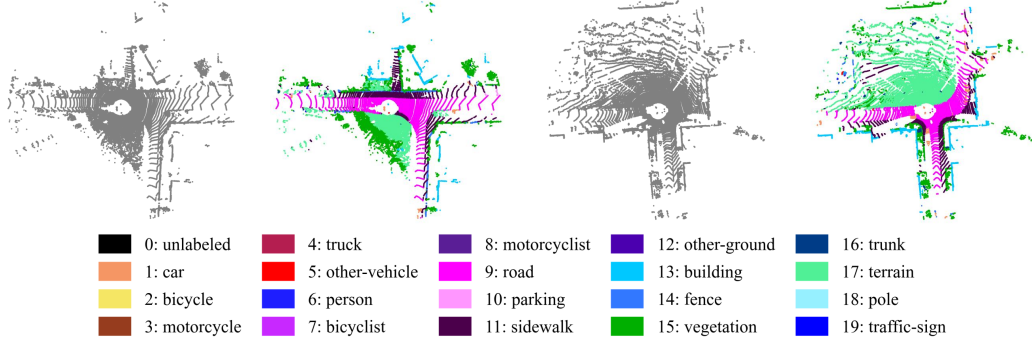


Figure 7: Details of semantic point cloud.

The OpenStreetMap (OSM) data is processed through a structured pipeline to generate georeferenced semantic representations. The raw OSM metadata, comprising area features (e.g., buildings, parks), way features (e.g., roads, fences), and node-based points of interest (POIs), is first categorized according to the hierarchical classification detailed in Tab. 6. Each element is projected onto a local East-North-Up (ENU) coordinate frame and rasterized into a three-channel Cartesian grid with a fixed resolution of $\Delta = 50$ cm/pixel. As shown in Fig. 8, the OSM tiles preserve the semantic and geographic information.

Table 6: Details of OSM elements.

Type	Element
Areas	building, parking, playground, grass, park, forest, water
Ways	Fence, wall ,hedge, kerb, building outline, cycleway, path, road, busway, tree row
Nodes	parking entrance, street lamp, junction, traffic signal, stop sign, give way sign, bus stop, stop area, crossing, gate, bollard, gas station, bicycle parking, charging station, shop, restaurant, bar, vending machine, pharmacy, tree, stone, ATM, toilets, water fountain, bench, waste basket, post box, artwork, recycling station, clock, fire hydrant, pole, street cabinet

A.2 Complementary Datasets

The KITTI [44] dataset contains LiDAR scans collected from urban driving trajectories in Karlsruhe, with poses provided by integrated GPS/IMU systems. To avoid overlap between training and testing regions, we use sequences 01, 02, 04, 05, 06, and 08 for training, and sequences 00 and 07 for testing. Sequence 03 is excluded due to missing pose information.

The KITTI-360 [45] extends the KITTI dataset with longer suburban routes. Following the former practice [15], synchronized sequences 00, 05, 06, and 09 are utilized for test. Statistics of query point cloud frames, osm tiles and trajectory length are available in Tab. 7.

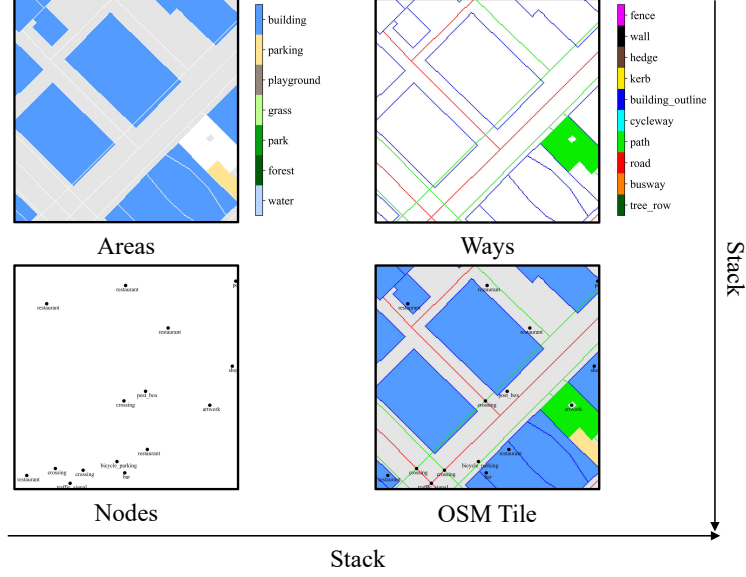


Figure 8: Illustration of areas, ways, nodes channels and full OSM tile.

Table 7: Statistics of test sets in KITTI and KITTI-360.

Dataset	KITTI		KITTI-360			
Sequence	00	07	00	05	06	09
Point cloud Frames	4541	1101	10514	6291	9186	13247
OSM Tiles	8782	3332	12491	15080	12730	13060
Trajectory Length (m)	8478	3226	11612	14541	12201	12570

B Implementation details

B.1 Loss function

Our OPAL employs a modified circle loss [50] for optimization. During training, for each query point cloud \mathcal{P} in a mini-batch, we consider its geographically matching OSM tile as the positive anchor \mathcal{O}_{pos} , while all other tiles beyond a negative distance threshold δ_{neg} meters serve as negative samples \mathcal{O}_{neg} . In the shared feature space of the global descriptor, the query point cloud should be close to the positive anchor and far from all the negative anchors. The similarity between a query point cloud descriptor \mathbf{d}_P and an OSM tile descriptor \mathbf{d}_O is measured through cosine similarity.

$$s = \frac{\langle \mathbf{d}_P, \mathbf{d}_O \rangle}{\|\mathbf{d}_P\| \|\mathbf{d}_O\|}. \quad (9)$$

The optimization objective simultaneously maximizes the similarity s_{pos} between queries and their positive anchors while minimizing similarities s_{neg} with negative samples. The optimization objective is defined as:

$$\mathcal{L} = \log \left[1 + \sum_{i=1}^{|\mathcal{O}_{neg}|} \exp(\gamma \alpha_n^i (s_{neg}^i - \Delta_{neg})) \cdot \exp(-\gamma \alpha_p (s_{pos} - \Delta_{pos})) \right] \quad (10)$$

where $\alpha_{neg} = \max(0, s_{neg} + \Delta_{neg})$ and $\alpha_{pos} = \max(0, 1 + \Delta_{pos} - s_{pos})$ are dynamic weights for hard negative and positive mining respectively. The hyperparameters Δ_{pos} and Δ_{neg} establish safety margins in the embedding space, while γ is a scaling factor controlling gradient sensitivity.

B.2 Parameters setting

Point clouds are filtered to retain points between 3m \sim 50m range, and OSM tiles are size of $H \times W = 100\text{m} \times 100\text{m}$. OSM tiles are sampled on GT positions during training and uniformly sampled along the trajectories with 1m interpolation during evaluation. The polar representation is size of $R = 480$ rings and $P = 360$ sectors. In the loss function, positive margin Δ_{pos} , negative margin Δ_{neg} , negative distance threshold δ_{neg} and scale factor γ in the loss function are set to 0.2, 1.8, 10 and 10, respectively.

C Additional Results

We provide extensive qualitative results on the KITTI and KITTI-360 datasets, as shown in Fig. 9. Compared with both hand-crafted methods [15, 46] and learning-based method [25], our method achieves more accurate and robust performance in diverse scenarios.

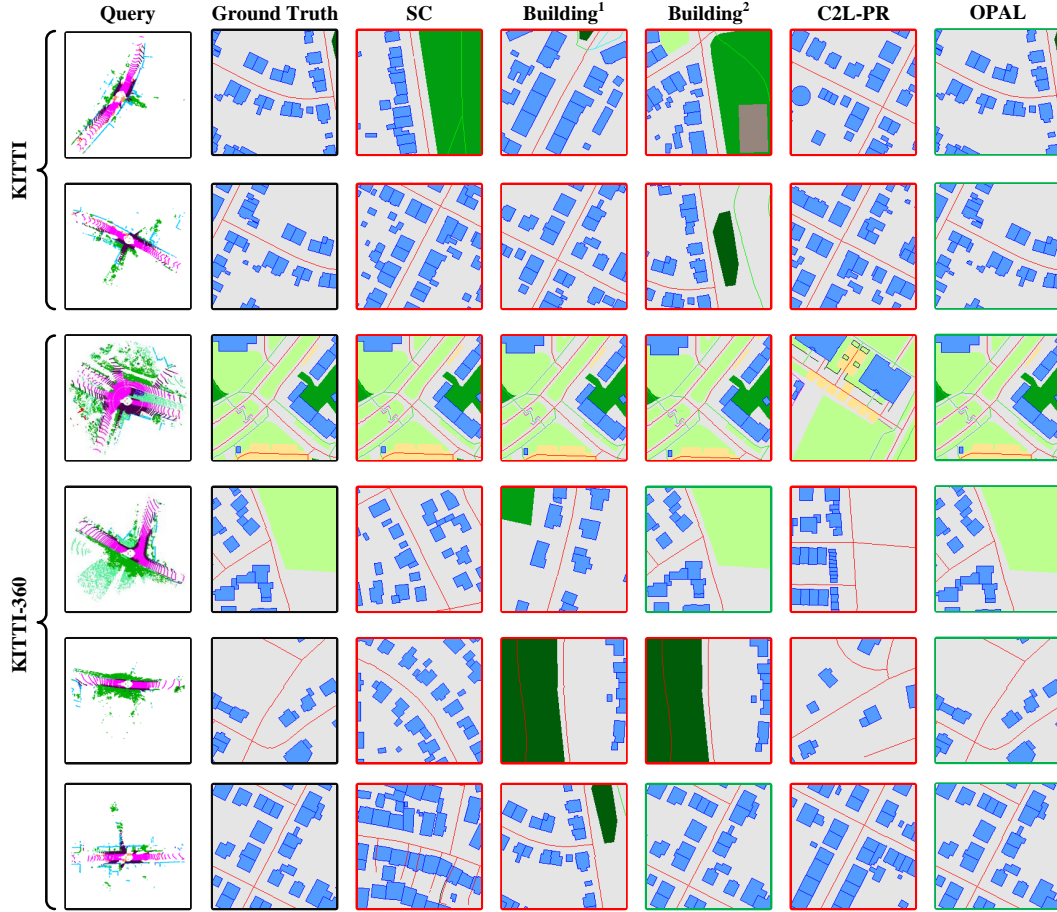


Figure 9: Examples of Lidar queries and their top-1 retrieved matches on KITTI and KITTI-360 dataset.